Multiscale Analysis of a Meso-β Frontal Passage in the Complex Terrain of the Colorado Front Range

LISA S. DARBY, WILLIAM D. NEFF, AND ROBERT M. BANTA

National Oceanic and Atmospheric Administration/Environmental Research Laboratories/Environmental Technology Laboratory, Boulder, Colorado

(Manuscript received 13 January 1998, in final form 27 July 1998)

ABSTRACT

Data from a mesoscale observing network are used to describe the evolution of a complex boundary between a dry air mass near the foothills of the Rocky Mountains and a shallow moist air mass over the eastern plains. Synoptic-scale analyses revealed that the origin of the moist air mass was associated with lee cyclogenesis. Mesoscale analyses provided a detailed picture of a localized anticyclonic circulation that developed within the larger-scale flow. Mixing ratio data from the mesoscale observing network indicated the position of the boundary between the air masses. It is shown that the cooler, moister air on the plains advanced toward and retreated away from the foothills during the evening. Eventually, downslope winds that were opposing the motion of the mesoscale boundary decreased, and the anticyclonic circulation on the plains became more organized. On an even smaller scale, Doppler lidar measurements revealed characteristics of the wind flow associated with the mesofront and the interaction of this flow with the downslope winds near the foothills of the Rocky Mountains. These characteristics included the horizontal variability of the winds near the complex foothills topography; the vertical structure of the winds associated with the mesofront, which indicated density-current-like features; the vertical structure of strong downslope flow opposing the mesofront's motion; and differences in the aerosol content of the air masses.

1. Introduction

The interaction of synoptic weather systems with mountainous terrain has long been recognized as the source of a variety of complex mesoscale phenomena. One of these phenomena is the occurrence of shallow cold fronts in the lee of the Rocky Mountains. In past studies, surface networks have provided some insight into the generation and propagation of these airmass boundaries. However, few instruments have been available to describe and diagnose their three-dimensional structure.

On the night of 17–18 February 1991, during a period of weak lee cyclogenesis, a shallow mesoscale cold front moved from the Colorado plains toward the foothills of the Rocky Mountains. This mesofront passed over the Rocky Flats Plant (RFP), a Department of Energy (DOE) facility, northwest of Denver, Colorado (Fig. 1a). An unusual feature of the event was that the shallow layer of cool easterlies behind the mesofront moved westward into the foothills despite an opposing strong westerly wind regime. Fortunately, this event occurred during a comprehensive deployment of remote and in situ sensors, which was being operated to obtain data to validate emergency response models for this DOE facility [see Elderkin and Gudiksen (1993) for an overview of the experiment].

The instrument deployment included the National Oceanic and Atmospheric Administration (NOAA) Environmental Technology Laboratory's (ETL's) Doppler lidar and array of 915-MHz wind profilers. The NOAA Forecast Systems Laboratory's (FSL's) surface-station network (mesonet) provided supporting data. Together, these instruments obtained detailed measurements of the mesofront and the meteorological conditions before and after its passage. The 915-MHz wind profilers provided hourly wind profiles as high as 4 km above mean sea level (MSL), from sites extending from near the Continental Divide to the plains. The resulting data characterized the larger-scale environment in which the event developed.

The Doppler lidar, which had a horizontal range of about 15 km under wintertime Front Range conditions, was located about 10 km east of the foothills. This position allowed detailed measurements of the propagation and structure of the mesofront as it impinged upon the sloping terrain near the foothills and then progressed into adjacent canyons. Fortunately, the absence of clouds in this particular mesofront allowed the lidar to probe its structure without obstruction. Additional sup-

Corresponding author address: Lisa S. Darby, NOAA/ETL, R/E/ET2, 325 Broadway, Boulder, CO 80303.

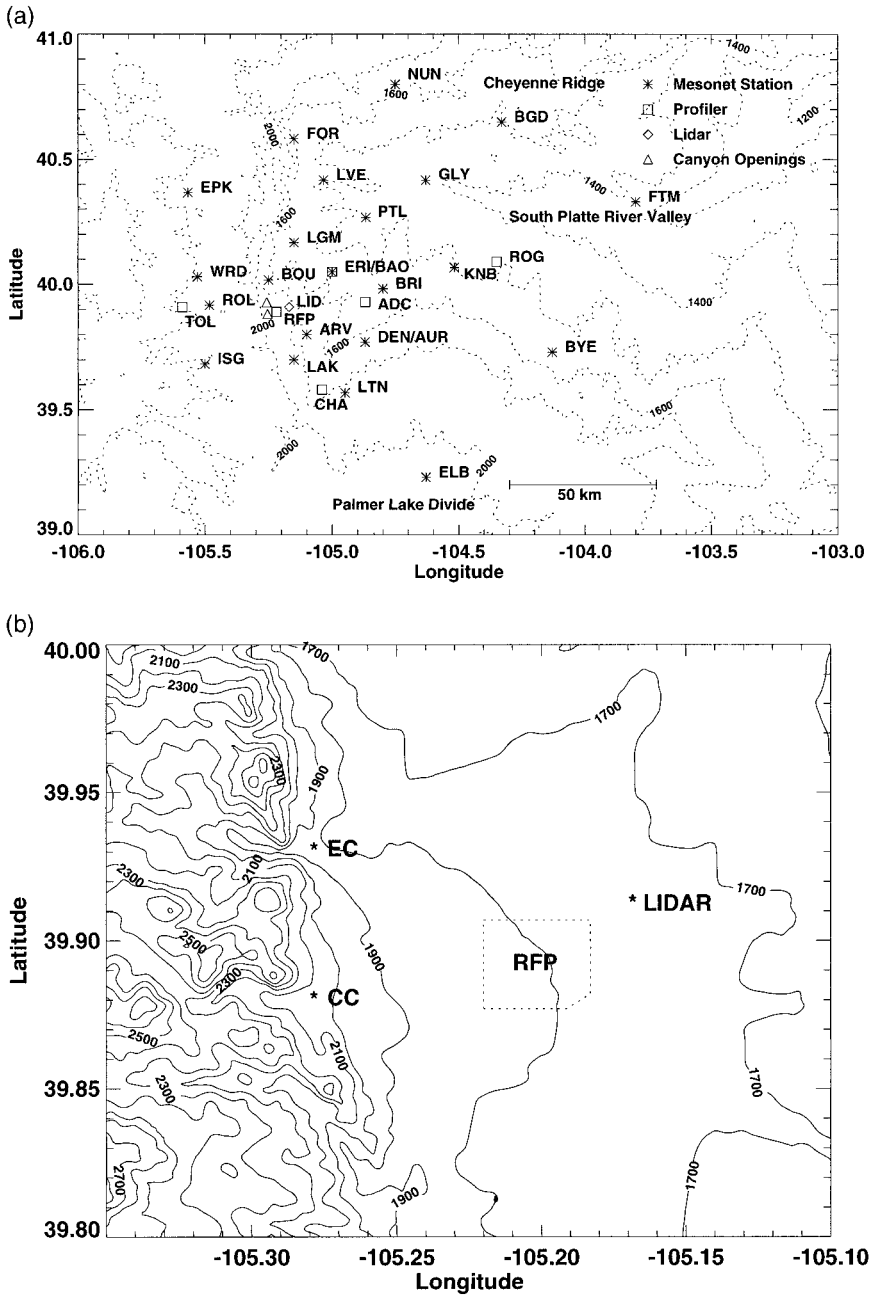

FIG. 1. (a). Terrain map of the Front Range of Colorado. Terrain contours are in 100-m increments from 1200 to 1700 m (MSL), and then 1000-m increments from 2000 to 4000 m (MSL). FSL mesonet station locations are represented by asterisks, squares are ETL profiler locations, and the lidar location (LID) is shown as a diamond. The triangle to the northwest of the lidar is the approximate location of the opening of Eldorado Canyon, and the triangle to the southwest is the approximate location of the opening of Coal Creek Canyon. The RFP tower was collocated with the RFP profiler. (b) A higher-resolution map showing the complexity of the terrain west of the lidar, including Eldorado Canyon (EC) and Coal Creek Canyon (CC). Terrain contours are in 100-m increments. The dashed lines indicate the boundaries of RFP.

porting measurements were available from a sounding system collocated with ETL's Doppler lidar.

Section 2 summarizes a number of past studies that have provided insights into synoptic-scale fronts occurring along the Colorado Front Range and their mesoscale features. Section 3 outlines the unique combination of instruments used to observe and describe the events of 17–18 February 1991. Section 4 presents de-

tailed lidar measurements of the winds before, during, and after the mesofront passage. In particular, high-resolution Doppler lidar measurements document the structure of the mesofront and its behavior as it interacted with the foothills terrain and downslope winds. Supporting data from the FSL mesonet are used in the analysis. Section 5 describes the synoptic environment, including the origin of the contrasting air masses lying over the plains, and suggests possible mechanisms underlying the origin of this mesoscale frontal event. Section 6 then focuses on the mesoscale environment, integrating profiler data, potential temperature and mixing ratio patterns, and streamlines. The evolution and effects of the mesofront are summarized in section 7.

2. Background

In previous research, both dry and moist synoptic-scale cold fronts have been observed in detail as they passed the Boulder Atmospheric Observatory (BAO, Fig. 1a) (Shapiro 1984; Young and Johnson 1984). Using Taylor's hypothesis, analyses of measurements from fast-response instrumentation on a 300-m tower gave finescale information on the structure and propagation of cold fronts, particularly the narrowness of the lowest 300 m of a front [the strong gradient of potential temperature, an indicator of frontal width, was only 170 m wide in Shapiro (1984)] and the abrupt changes in temperature and winds accompanying the passage of a front (Young and Johnson 1984). Young and Johnson (1984) found that because the western side of the Cheyenne Ridge, in northern Colorado, has higher terrain elevations than its eastern portion (see Fig. 1a), the colder air behind their synoptic-scale front reached the Colorado foothills hours after the cold front moved southward over the eastern plains of Colorado, underscoring the importance of this terrain feature. In these early papers, surface mesonet stations provided information about the motion of the fronts on the plains, but the interaction between the colder air behind the fronts and the complex terrain of the foothills was not observed.

In other work, Doppler and monostatic sodars and a Doppler lidar from NOAA/ETL were used during the 1987–88 Denver Brown Cloud Study (DBCS). In addition to the permanent array of Front Range instrumentation and chemistry measurements, the sodars and lidar were used to document meteorological conditions in the South Platte River Valley conducive to high-pollution episodes (Neff 1990). The wintertime regime of upvalley flow during the day and down-valley flow during the night was well documented. High-resolution profile measurements of these along-valley flows by sodars provided new information, particularly the existence of dynamically driven, upvalley flows and small-scale fronts similar to those observed at the leading edge of gravity currents (Neff 1990). Neff (1997), who compared independent model results and observations from the DBCS, found evidence of small-scale cold fronts that were also associated with aged pollution, moving upvalley into Denver.

Davis (1995) analyzed another class of frontlike event, referred to as a mesoscale cold surge, which was marked by an increase in wind velocity and a brief snow storm in the Denver metropolitan area. This occurred ahead of a synoptic-scale cold front and was first observed at the Cheyenne, Wyoming, weather station, on the Cheyenne Ridge. Model simulations indicated that this feature was a topographic wave modified by uneven heating along the Front Range, specifically, the heating of the Cheyenne Ridge. The heating of the ridge increased the Froude number of the flow, allowing the air to flow over the ridge and consequently across the plains of Colorado, ahead of the synoptic-scale cold front.

Davis (1997) analyzed two types of leeside anticyclones that form south of the Cheyenne Ridge, along the Colorado Front Range. Potentially colder air is advected from the plains toward the mountains by the mesoscale anticyclonic flow. In an FSL mesonet station plot, traces of potential temperature, wind speed and direction, and pressure perturbation clearly show the passage of a cold front, the only evidence of a front presented in the study. Davis's paper focuses on the dynamics of the leeside circulation, with the cold air advection mentioned as a feature resulting from the anticyclonic flow. In the following study, we show the details of the structure of the resulting mesoscale cold front associated with the leeside anticyclonic circulation.

This past work demonstrates that the occurrence of small-scale fronts and finescale features of synoptic-scale cold fronts have been well documented along the Front Range of Colorado by a variety of instruments and that they have a significant impact on local weather and air quality. However, the location and breadth of the instruments involved in these previous experiments limited their ability to observe the behavior of these fronts as they approached the foothills of the Rocky Mountains, particularly their three-dimensional structure and evolution. Of particular value in the current study is the array of remote and in situ instruments used to describe the mesofront's motion, vertical structure, and interaction with larger-scale flows.

3. Instrumentation

a. Doppler lidar

The NOAA/ETL Doppler lidar used in this study is a laser-based remote sensing instrument that simultaneously measures range-gated, backscattered signal intensity and radial wind velocity (Post and Cupp 1990). Pulsed light at a wavelength of 10.59 μm is emitted. Atmospheric aerosols suspended in the clear air scatter part of the light back to the lidar. The frequency shift of the returned radiation, which is due to the wind-driven motion of the aerosols, is detected and used to

determine the radial component of the wind. The quantity, size, shape, and chemical composition of the aerosols affect the lidar's signal strength. At a wavelength of 10.59 μm, most scattering occurs by particles 1–3 μm in diameter. Since water vapor absorbs energy from the laser beam, the lidar performs better in a dry atmosphere. Examples of the types of research to which lidar is well suited include the evolution of the Monterey Bay sea breeze (Banta et al. 1993a; Banta 1995), fluctuations in stratospheric aerosols due to the volcanic eruptions of El Chichón and Mount Pinatubo (Post 1986; Post et al. 1992), visibility studies in the Grand Canyon (Banta et al. 1999), ice-cloud depolarization (Eberhard 1992), and the structure of the winds and smoke distribution in the plume of a prescribed forest fire (Banta et al. 1992).

Because its beam is narrow ($\sim$90 μrad), the lidar can scan close to the ground and into narrow valleys or canyons with an along-beam resolution of 300 m. Two basic types of scan are plan position indicator (PPI) and range–height indicator (RHI) scans. During a PPI scan, the scanner remains at a constant elevation angle while sweeping in azimuth. When sweeping through a full 360° in azimuth, a cone of measurements is obtained. This type of scan is useful for seeing the spatial variability of winds and aerosols. During an RHI scan, the scanner remains at a constant azimuth while varying in elevation, obtaining a vertical slice of measurements in the atmosphere. RHI scans yield valuable information about the vertical structure of winds and aerosols, and because of the narrow beam, vertical resolution is high. During both types of scan, the scanning speed can be controlled, resulting in higher- or lower-resolution measurements. A series of PPI or RHI scans with a small change in constant angle between sweeps provides a three-dimensional volume of data.

For this study, high-resolution three-dimensional volume scans measured the flow over the RFP and along the complex terrain of the foothills of the Rockies. For this type of scan, the scanner moved between 225° and 305° in azimuth and from 0° to 5° in elevation, incrementing every 0.2° in elevation. The data from these scans were edited by removing range gates contaminated by terrain and then transforming the measurements from spherical to Cartesian coordinates.

During this case study, a routine series of low-elevation angle PPI scans detected a distinct wind-shift line between downslope westerlies and northeasterlies, indicating the presence of the mesofront. RHI scans measured the flow over the plains and in the two nearby canyons. From RHI scans, the u component of the wind, that is, the horizontal wind component along the plane of the RHI, was calculated by first interpolating the radial velocity measurements from polar to Cartesian coordinates and then, assuming the flow was nearly horizontal, by dividing the radial velocity, u_r, by the cosine of the elevation angle. Using a centered-differencing method, the u component of the wind was used to create a divergence field. An upward integration of the divergence field was then performed to derive a vertical velocity, w, field by assuming mass continuity. Two other assumptions were made: 1) $w = 0$ at the surface and 2) the cross-beam divergence was negligible.

The combination of PPI and RHI scans performed by the lidar obtained a comprehensive view of the wind conditions within a 15-km radius of the RFP before, during, and after the mesofront passage, with a spatial resolution unobtainable by any of the other instruments or network of instruments involved in the study (Banta et al. 1993b).

b. Mesonet

FSL's 22-station network of meteorological instruments continuously recorded 5-min averages of surface temperature, dewpoint, wind speed and direction, solar radiation, and precipitation. This network, called the FSL mesonet, stretched along the Front Range of Colorado (Fig. 1a) from Nunn (NUN) at the north end of the network to the Palmer Divide (ELB) at the south end, and extended from the mountains to 150 km out on the plains.

The FSL mesonet contributed valuable information about the small-scale features along the Colorado Front Range that were missed on the synoptic-scale maps. For example, only the stations close to the foothills and south of Loveland (LVE) detected the mesofront. The passage of the mesofront was measured at these stations as a shift to easterly winds, a drop in temperature, and an increase in moisture.

c. The 915-MHz profiler network

Six 915-MHz radar wind profilers (Ecklund et al. 1988) deployed by ETL obtained wind profile measurements continuously throughout the experiment. These instruments operate virtually unattended and their measurements of radial Doppler shifts are averaged and converted into hourly wind profiles. The 915-MHz wind profilers have been used successfully in several air quality studies in complex terrain, as summarized by Neff (1994).

Using fluctuations in the microwave index of refraction—which is dominated by humidity—as a scattering medium, the profilers operate simultaneously in high-resolution and low-resolution modes. The high-resolution mode has a range resolution of 100 m in the vertical, with a maximum range of 2–3 km depending on atmospheric conditions. Greater depths of moist air provide greater ranges. The low-resolution mode has a range resolution of 400 m in the vertical, with a maximum range of 4–5 km. The minimum range during this study was 120 m above ground level (AGL).

Because the profilers operated continuously, they offered a time series of the wind velocity before, during, and after the mesofront event. Measurements up to 4

km MSL in the vertical showed the structure of upper-level winds. With five profilers on the plains and one in the mountains (Fig. 1a), the profiler measurements revealed the spatial diversity of winds during the event.

d. Supporting data

The RFP operates a 61-m tower on the western boundary of the site, near the foothills. The tower is instrumented at three levels: 10, 25, and 60 m. Instruments at the 25-m and 60-m levels measure wind speed and direction, temperature, and vertical velocity. The 10-m level measures these same parameters plus pressure, dewpoint, and precipitation. Data are recorded in 15-min averages, with the maximum, minimum, and standard deviation for each 15-min period also recorded. The RFP tower measurements clearly showed the passage of the mesofront. Collocated with the Doppler lidar at the northeast corner of the RFP, a balloon-borne sounding system provided temperature and humidity profiles. Just prior to the event, an airsonde had been launched. With the approaching mesofront visible at the maximum range of the lidar, a second airsonde was prepared and launched just after the mesofront passage at the lidar site.

4. Detailed measurements of mesofront passage

a. Premesofront

Prior to the mesofront passage, lidar observations concentrated on canyon winds and the horizontal variability of the flow along the foothills. A series of nearly horizontal (0.5° elevation) Doppler lidar scans that began just before 0200 UTC 18 February 1991 showed the evolution of prefrontal downslope winds to postfrontal upslope winds (Fig. 2). The first scan (0152 UTC; Fig. 2a) showed west-northwesterly winds flowing to the southeast of the lidar and RFP. The 915-MHz profiler at RFP (Fig. 3b) showed a northwest wind of $\sim$12 m s^{-1} from 2 km to 3.5 km MSL at 0200 UTC, in close agreement with lidar measurements. The 10-, 25-, and 60-m levels of the RFP tower (Fig. 4) indicated northwesterly winds of 13–17 m s^{-1} at 0200 UTC and temperatures of $\sim$2°C. These measurements indicate that the wind field over RFP was fairly homogeneous at this time. The consistency of the wind measurements with height implied that the winds aloft (above mountaintop) were coupled to the winds at the surface, indicating the absence of a cold air layer at the surface. This showed that the Eldorado Canyon exit flow was not a thermally driven drainage flow, but an ambient northwest flow focused by the canyon (Banta et al. 1995).

Figure 5a, taken from a high-resolution lidar scan beginning at 0327 UTC, indicated westerly flow. The structure of the wind was similar to that seen in Fig. 2a, with velocity maxima $>$14 m s^{-1}. These maxima were described in Banta et al. (1995) as possibly being the result of high-momentum air reaching the ground due to wave activity. Plots depicting the vertical structure of the flow out of Eldorado Canyon before the mesofront reached the lidar and just after the measurements in Fig. 5a are shown in Fig. 6. Figure 6a is a contour plot of the u component of the wind and shows strong down-canyon flow with a wind speed maximum of 12 m s^{-1}. In Fig. 6b, a vector plot of the u and w components of the wind, high-frequency wavelike structure is clearly seen. A similar high-resolution vertical scan directed toward Coal Creek Canyon showed almost the same structure in the winds. Overall, the premesofront wind pattern, as shown in detail by lidar measurements, consisted of strong downslope west-northwesterlies with areas of stronger winds near the surface, presumably resulting from upstream terrain effects.

b. Mesofront passage

1) FINESCALE STRUCTURE

Between 0400 and 0500 UTC, the mesofront passed through the RFP region, changing the winds, temperature, and moisture content of the lowest few hundred meters of the atmosphere. The mesofront passage at the RFP tower was seen most distinctly in the wind direction and mixing ratio plots at 0500 UTC (Fig. 4). The wind direction abruptly switched from northwesterly to easterly while the mixing ratio jumped from 1.8 to 3.6 g kg^{-1}. It was clear from tower and mesonet data that a change in mixing ratio, in addition to a wind shift, was a strong indicator of the mesofront passage. In fact, mixing ratio was a better indicator of the different regional air masses than was potential temperature. Figure 7 shows a time series of potential temperature (solid lines) and mixing ratio (dashed lines) for seven mesonet sites where the mesofront passage occurred. In general, the change in moisture with the mesofront passage was more distinct at all of these stations than the change in potential temperature. The changes in wind direction that correspond to the changes in moisture can be seen in Fig. 8 (mesonet wind speed and direction time series for the same seven sites in Fig. 7). Lower mixing ratio values occurred with west to northwest winds while higher mixing ratio values occurred with northeast to east winds. At some stations, for example, Erie (ERI) and Denver/Aurora (Den/AUR), the moist air mass advanced and retreated as the wind direction shifted.

Shortly after 0400 UTC, a series of low-angle lidar PPI scans showed the distinct wind shift between the easterly flow behind the mesofront and the downslope northwesterlies. An example was shown in Fig. 2b, where the change in direction of the wind due to the mesofront appears as a shift from yellow to green radial velocities east and northeast of the lidar. Also, by this time the west-northwesterly winds were several meters per second weaker and the gusty structure was less pro-

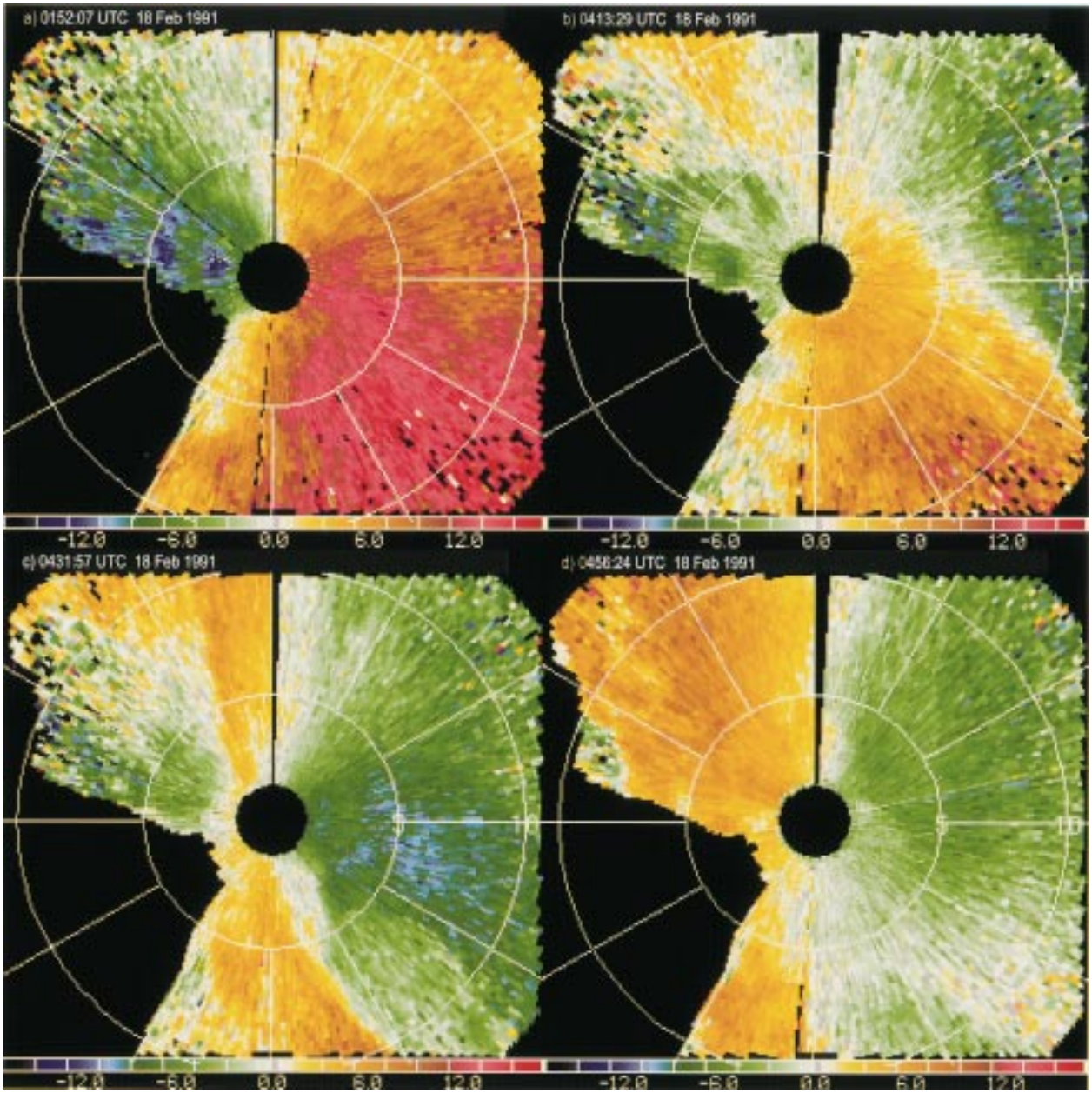

FIG. 2. Lidar-measured winds, in m s^{-1}. The lidar is located in the center of the plots; west is to the left of the scan and north is to the top; range rings are 5 km apart. Purple-green colors indicate flow toward the lidar while yellow-red colors indicate flow away from the lidar. (a) At 0152:07 UTC 18 Feb 1991 (1852:07 MST 17 February), strong, gusty winds up to 16 m s^{-1} were flowing toward the lidar, with the strongest winds flowing from the direction of Eldorado Canyon (~282° in azimuth; see Fig. 1b). (b) About 2.5 h later, the west-northwesterly winds had weakened by several m s^{-1}, and the wind shift line between the northeasterlies behind the mesofront and the downslope winds was distinct. (c) The downslope flow continued to weaken as the mesofront passed the lidar. (d) About 15 min later, the wind flow near the surface had completely changed direction from earlier in the evening.

nounced than in Fig. 2a. The Tolland (TOL) (Fig. 3a) and RFP (Fig. 3b) profiler wind measurements showed a decrease in wind speed aloft (above 3.3 km MSL) in the hours preceding the mesofront passage, which may be related to the weakening of the downslope winds in the vicinity of RFP. In particular, winds measured by the RFP and Chatfield (CHA) profilers decreased throughout the whole profile from between 0200 UTC and the mesofront passage. Figure 2c, a scan taken just ~15 min after the scan shown in Fig. 2b, showed the mesofront at the lidar site with strong easterlies behind it, and even weaker winds flowing from the west-northwest.

Lidar measurements from 0419 to 0436 UTC (Fig.

9) show the vertical structure and propagation of the mesofront as it approached and passed the lidar. In Fig. 9 the scans were aligned nearly perpendicular to the mesofront and along its direction of propagation. The mesofront (seen as a convergence zone 3 km east-northeast of the lidar) and the westerly flow overriding the cooler easterly flow behind the mesofront were evident in Fig. 9a. In Fig. 9b, just 2 min later, the front was closer to the lidar and the head region had steepened. By 0436 UTC (Fig. 9c) the front had passed to the west-southwest of the lidar.

After the mesofront passed the lidar site, high-resolution vertical scans toward both Coal Creek and Eldorado Canyons were performed, documenting the structure of the mesofront as it approached the foothills. Figure 10 shows a vector plot of the u and w components of the wind and contours of range-corrected backscattered signal intensity, called ''intc,'' from the high-resolution scan pointing into Eldorado Canyon. The plots show the easterly flow behind the front meeting the westerly downslope flow between 6 and 7 km west-northwest of the lidar. An important feature is the difference in intc, arbitrary numbers in decibels (dB), between the two air masses. Lower intc values indicate cleaner air, so the air exiting the canyon was much cleaner than the air behind the mesofront. Plots from the scan pointing into Coal Creek Canyon (not shown) revealed similar structure. This finding has implications for air quality issues in the Denver metropolitan area. Pollutants that have settled into the South Platte River Valley or have been previously transported to the east may be brought back into the metropolitan area by a mesofront similar to the one documented here. However, because of the increased relative humidity in the air mass behind the front, hygroscopic aerosols could also grow, creating stronger lidar signals.

A sounding launched from the lidar site at 0400 UTC (Fig. 11) showed a shallow temperature inversion at the surface and a rapid decrease in temperature with height. The mixing ratio was between 1 and 2 g kg^{-1}, fairly uniform with height. A second sounding (Fig. 11) was launched from the lidar site after the mesofront passed through the area, about 45 min after the first sounding. The mesofront passage brought a temperature drop of $\sim$4°C and a mixing ratio increase of $\sim$2 g kg^{-1} near the surface.

2) DENSITY CURRENT

The vertical structure of the mesofront, as seen in contours of u (Fig. 9), and changes in potential temperature and moisture coinciding with the mesofront passage (Fig. 7), suggested that the mesofront had the characteristics of a density current. The propagation speed c of a density current can be defined as (Bluestein 1993)

$$c = K\left(\frac{\Delta p}{\rho_w}\right)^{1/2} + 0.62\overline{u}, \tag{1}$$

where K is a Froude number, $\Delta p = p_c - p_w$ is the difference in surface pressure between the colder and warmer air, ρ_w is the density of the warmer air, and $\overline{u}$ is the vertically averaged speed of the ambient flow through a depth equal to that of the colder air. Internal Froude number K measures the phase speed of the internal wave relative to the ambient flow and can be used to indicate if an air mass has density current characteristics. Its theoretical value, based on idealized fluid flow, is $2^{1/2}$, but because of effects such as surface friction and mixing, K is smaller for atmospheric density currents (Koch et al. 1991). Values of K associated with density currents range from 0.8 to 1.1 (Koch et al. 1991), or 0.7 to 1.1 (Bluestein 1993) for thunderstorm-generated density currents. Rewriting (1) to estimate K from observational data gives

$$K = \frac{c - 0.62\overline{u}}{\left(\frac{\Delta p}{\rho_w}\right)^{1/2}}. \tag{2}$$

RFP tower and lidar measurements can be used in (2) to estimate K for the mesofront. Using the zero u contour as an indication of the mesofront boundary, and looking at the change of its surface position between 0419 UTC (Fig. 9a) and 0436 UTC (Fig. 9c), we estimated c to be 5.6 m s^{-1}. From 10-m-level RFP tower measurements (Fig. 4), one-half hour before and after the mesofront passage, the difference in surface pressure, Δp, was 1 mb = 100 Pa and the density of the warmer air, ρ_w, was 1.019 kg m^{-3}. The initial intrusion of easterly flow was $\sim$400–500 m deep, as seen in the zero u contour in the lidar data (Fig. 9). Behind the mesofront the depth of the colder air was estimated to be $\sim$600 m, as determined from 1) the temperature difference between the two soundings launched at the lidar site (Fig. 11), 2) the hourly averaged winds seen in the RFP profiler measurements (Fig. 3b), and 3) later lidar measurements. For example, in Fig. 12, a plot of u contours from a vertical scan in the direction of Eldorado Canyon, the easterly flow was $\sim$600 m deep. Thus the depth of the colder air ranged from $\sim$400 to 600 m.

Simpson and Britter (1980) found that when using atmospheric data, a vertical average of the ambient flow wind speed, $\overline{u}$ in (1), rather than a maximum value, was more consistent with their laboratory experiments. The lidar data shown in Fig. 9b lend themselves well to the calculation of $\overline{u}$, since a vertical average of the component of flow opposing the mesofront propagation can be easily obtained. A vertical average calculated from the surface to 600 m and $x = -4.5$ to -3.5 km gives $\overline{u} = -4.2$ m s^{-1}. The minus sign accounts for the fact that the ambient flow opposed the mesofront propagation. Using the above values for c, Δp, ρ_w, and $\overline{u}$ in (2) gives a value of $K = 0.83$. To

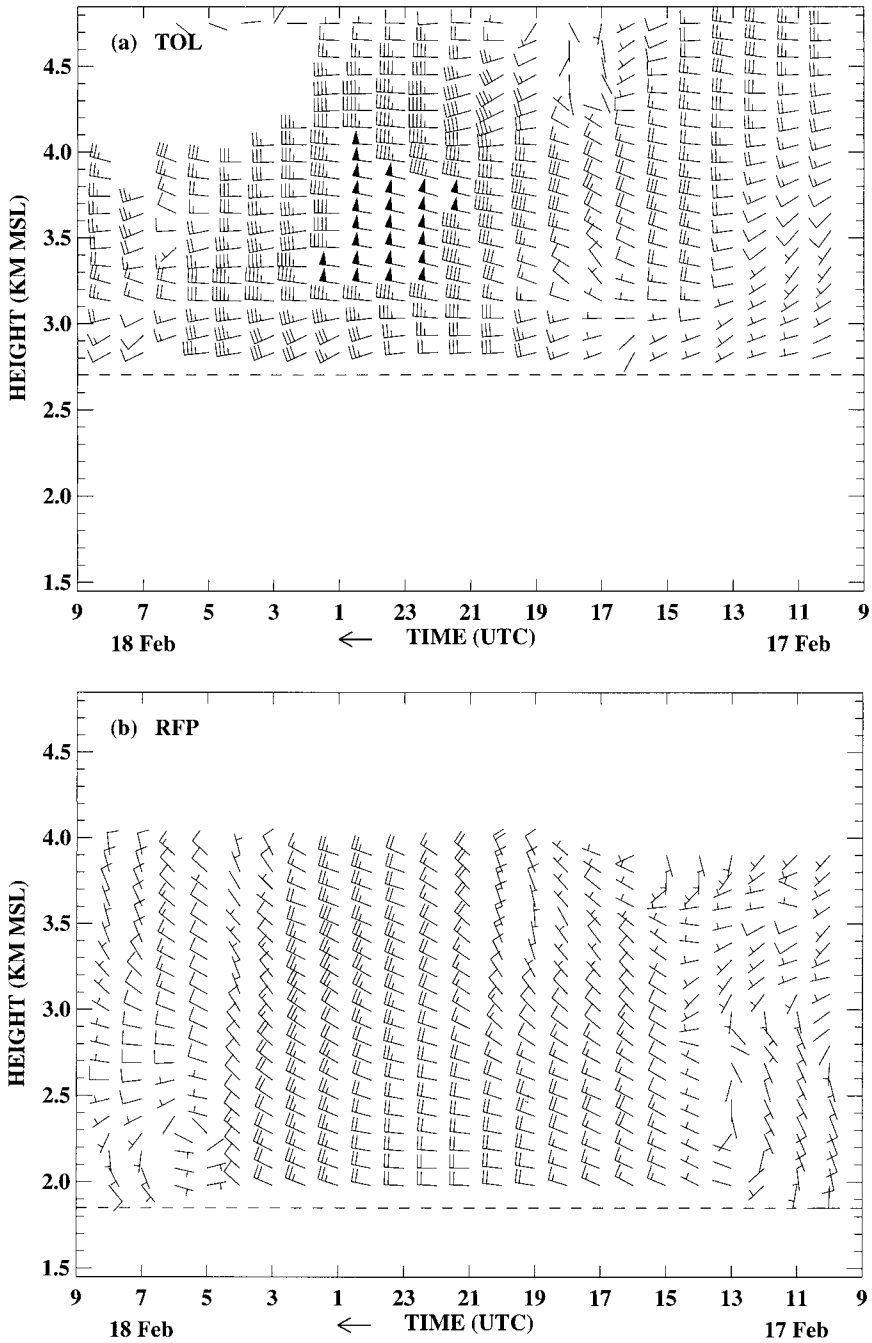

FIG. 3. Wind profiles from the 915-MHz profilers. The dashed line is station elevation. A half-barb is 2.5 m s^{-1}, a full barb is 5 m s^{-1}, and a pennant is 25 m s^{-1}. The sites are (a) Tolland (TOL) and (b) Rocky Flats Plant (RFP). Time runs from right to left.

account for any uncertainty in choosing the data region to calculate $\overline{u}$, K was calculated for $\overline{u} \pm 2$ m s^{-1}, yielding a range of values from $K = 0.83 \pm 0.13$, which is consistent with the density current range noted above.

Since the equation for c was developed under the assumption of a flat surface, a factor that may have increased the uncertainty in K is that the mesofront was traveling uphill as it crossed RFP. The propagation speed of ~6 m s^{-1} was much lower than the speed of other documented density currents, such as 10 m s^{-1} (Ralph et al. 1993), 12 m s^{-1} (Koch et al. 1991), or 20 m s^{-1} (Charba 1974). The terrain slope, ~0.016, plus a temperature difference between air masses of 4°C, has an equivalent pressure gradient of 100 Pa $(40 \text{ km})^{-1}$, comparable with that associated with a ~10 m s^{-1} geo-

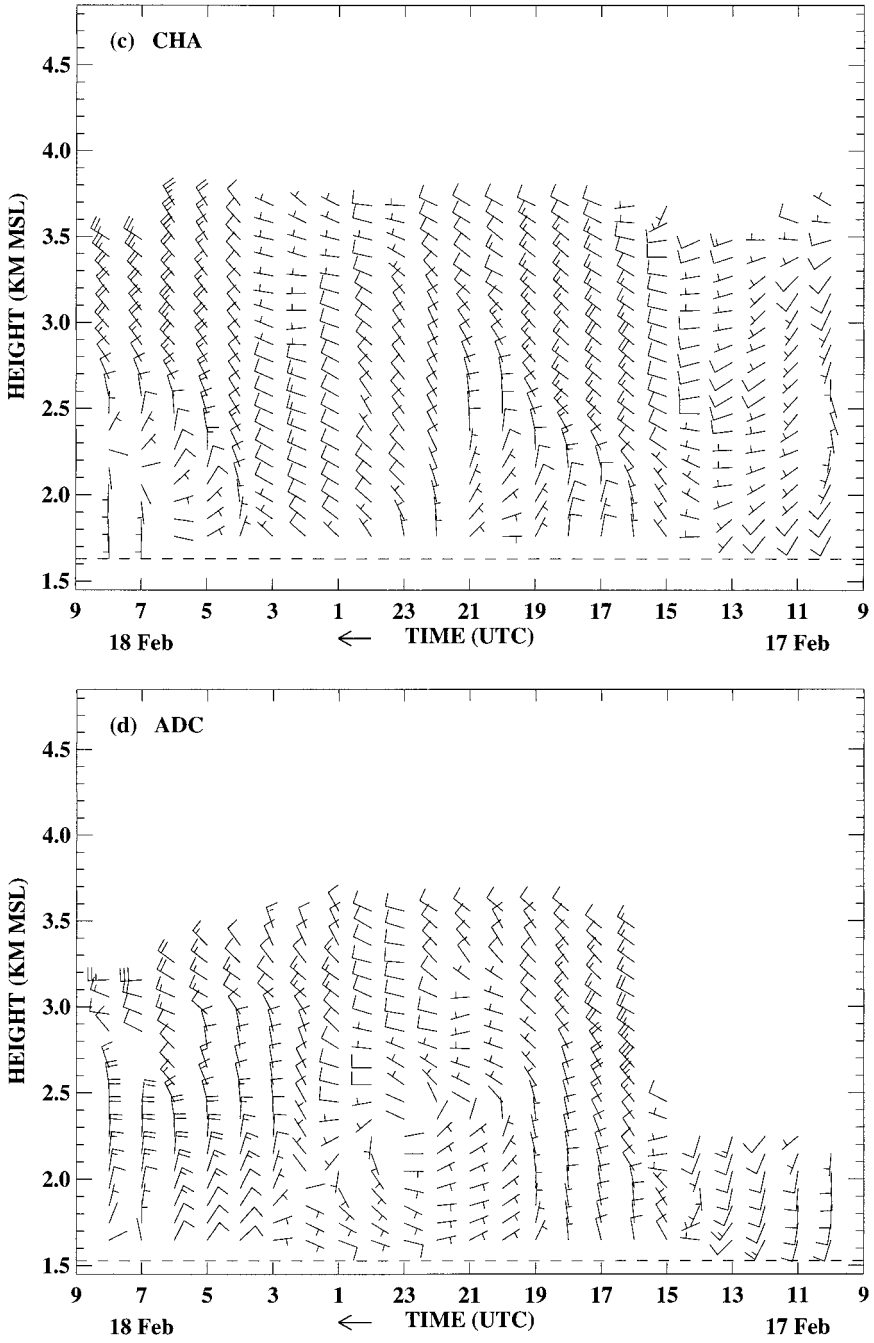

FIG. 3. (*Continued*) The sites are (c) Chatfield (CHA), (d) Adams County (ADC), and (e) Roggin (ROG). Time runs from right to left.

strophic wind (Neff and King 1987, see their Fig. 17). Without this effect, perhaps *c* would have been higher, yielding a higher value of *K*.

c. Postmesofront

The complete reversal of winds in the RFP region due to the passage of the mesofront is clearly seen when comparing Fig. 2a with Fig. 2d (0456 UTC). Except for a small region of westerly flow at ranges beyond 7 km in the beams aligned with Eldorado Canyon, the winds at the later time were easterly. The wind reversal was also seen when comparing Fig. 5a with Fig. 5b. Within just over 1.5 h, westerly winds with a maximum of 14 m s^{-1} had switched to easterly winds with a maximum of ~8 m s^{-1}.

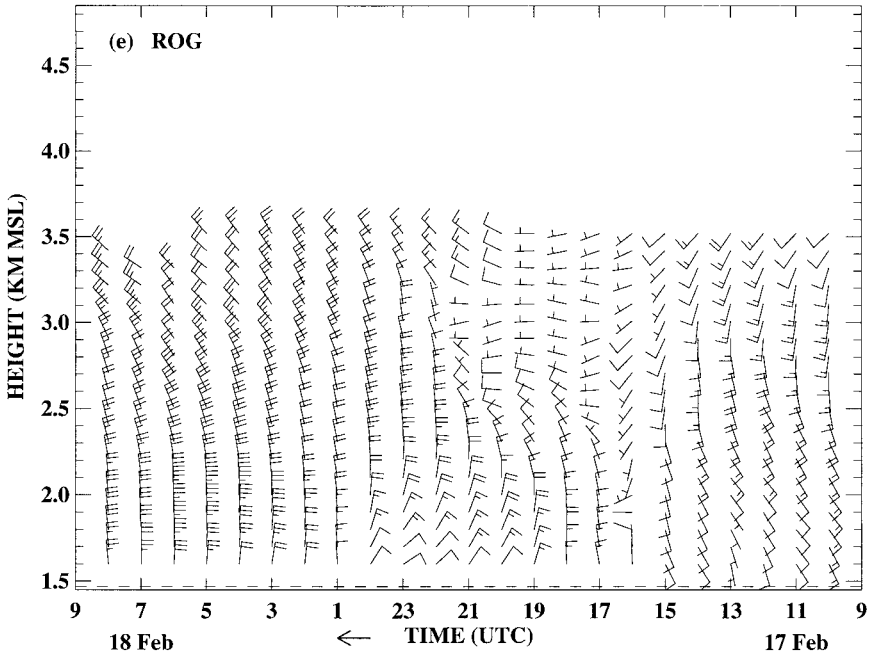

FIG. 3. (*Continued*)

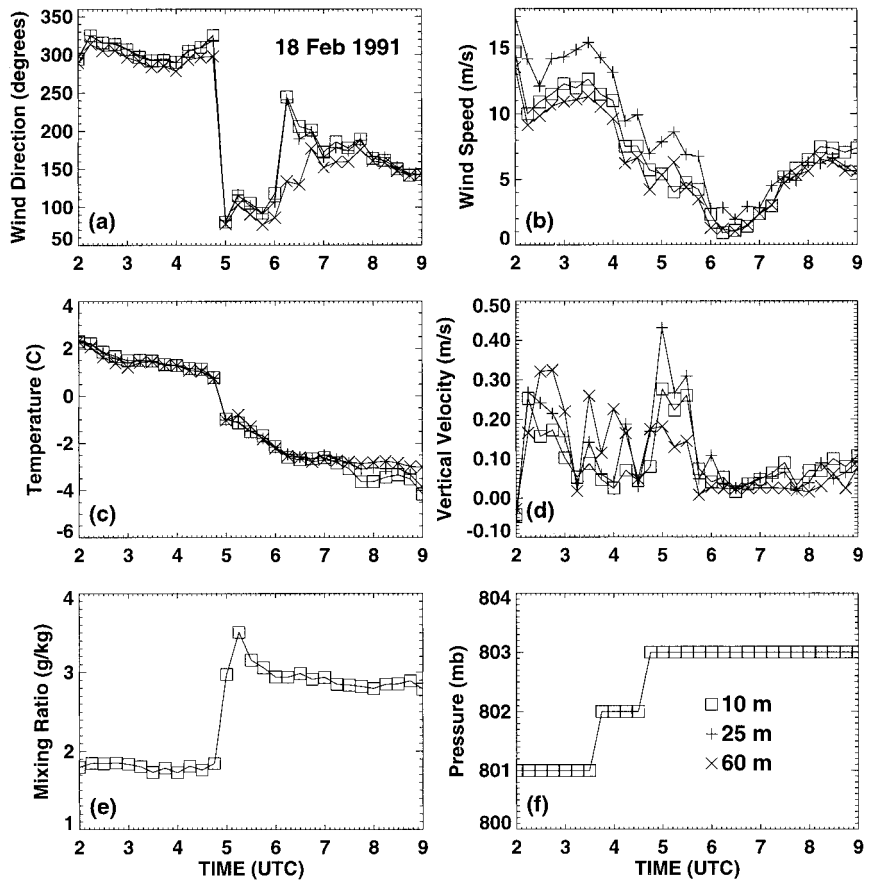

FIG. 4. Measurements from the Rocky Flats Plant tower: (a) wind direction (° from north), (b) wind speed (m s^{-1}), (c) temperature (°C), (d) vertical velocity (m s^{-1}), (e) mixing ratio (g kg^{-1}), 10-m level only, and (f) pressure (mb), 10-m level only.

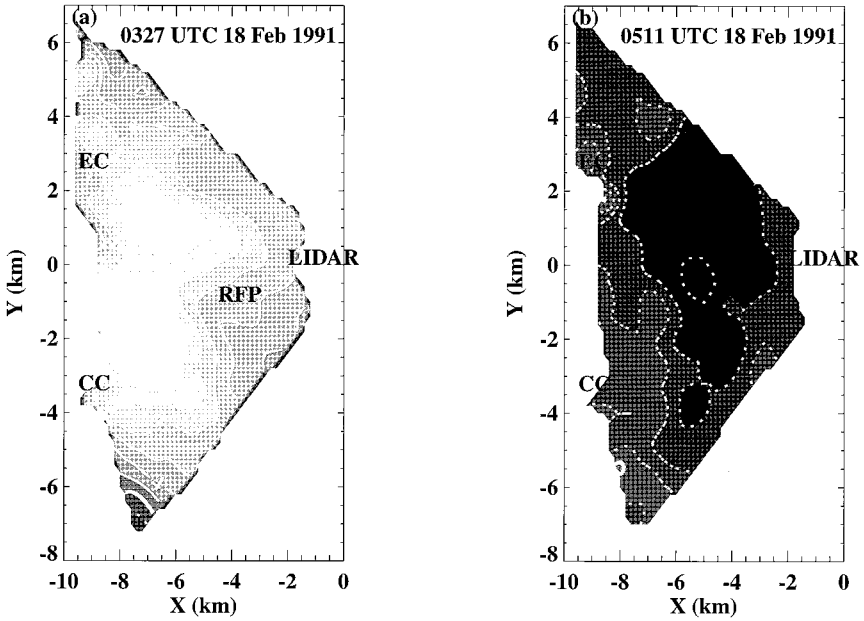

FIG. 5. Smoothed radial velocity contours in increments of 2 m s^{-1}. Solid lines (positive velocities) indicate flow toward the lidar, and dashed lines (negative velocities) indicate flow away from the lidar. The locations of the lidar, EC, CC, and RFP are indicated. The data are from a horizontal slice (300 m AGL) through a high-resolution scan (as described in section 3). Times indicate when the scans began: (a) 0327 and (b) 0511 UTC.

At 0630 UTC, both Coal Creek Canyon and Eldorado Canyon still had up-canyon winds because of the mesofront. The contour plot of the *u* component of the wind, the lidar pointing into Eldorado Canyon, showed the shallow layer of up-canyon flow ~600 m deep (Fig. 12). The residual westerly flow seen in Fig. 2d is seen in Fig. 12 as the westerly (solid) contours above 600 m.

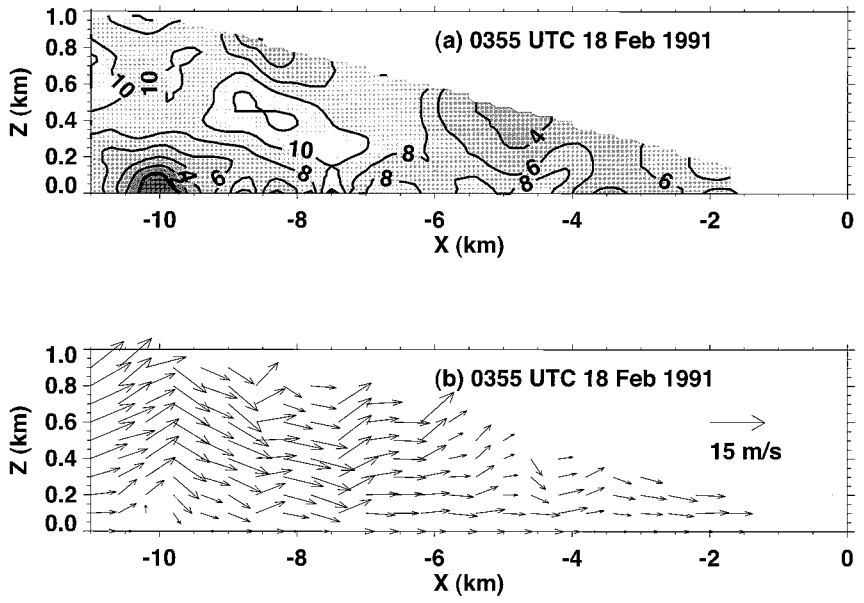

FIG. 6. (a) Smoothed contours of the *u* component of the wind and (b) a vector plot of the u_r and *w* components of the wind along the 282.5° radial, pointing into Eldorado Canyon. Solid contours represent flow with a westerly component. The lidar is located at (0, 0). The opening of Eldorado Canyon is at approximately $x = -10$ km.

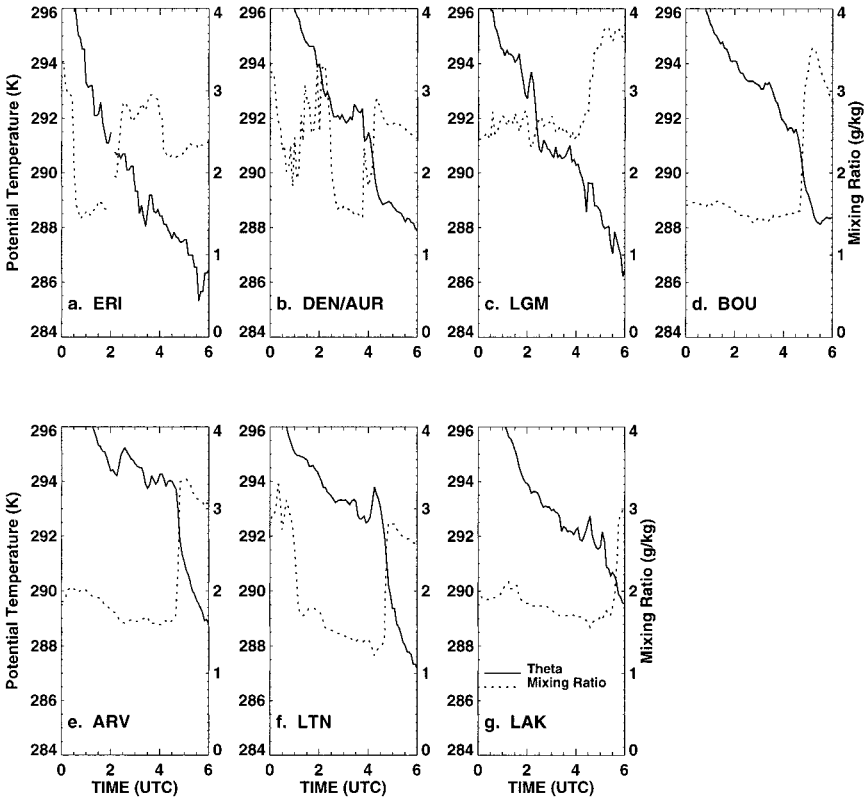

FIG. 7. Time series of potential temperature (solid) and mixing ratio (dashed) at seven mesonet stations: (a) ERI, (b) DEN/AUR, (c) LGM, (d) BOU, (e) ARV, (f) LTN, and (g) LAK.

Lidar, balloon, and mesonet station observations revealed that the mesofront was a shallow yet distinct feature that affected the winds, moisture, and aerosol content of the lowest few hundred meters of the atmosphere. Lidar and profiler measurements point to the possibility of a relationship between the passage of the mesofront and the decrease in winds aloft as well as the wave activity associated with these winds. In an attempt to understand what generated the mesofront, synoptic-scale and mesoscale analyses follow.

5. Synoptic environment for 17–18 February 1991

From 0000 UTC 17 February to 1200 UTC 18 February, the 300-, 500-, and 700-mb maps showed an intensifying upper-level trough in the western United States sloping westward with height. Upper air maps from 0000 UTC 18 February 1991, showing the slope of the trough with height, are presented in Fig. 13. Another synoptic feature, a surface stationary front extending along the northern Rockies and then stretching from Nebraska eastward, also dominated the synoptic weather pattern of the United States (Figs. 14a–e). The deepening and eastward motion of the upper-level trough, coupled with the surface trough along the eastern side of the Rocky Mountains, compose a classic case of lee cyclogenesis. Three weak low pressure systems formed, one after the other, on the plains of Colorado during the morning hours of 17 February (not shown). Eventually, a single surface low positioned over the Oklahoma Panhandle became a dominant leeside synoptic feature.

The Oklahoma Panhandle low was responsible for the advection of relatively warm, moist air onto the eastern plains of Colorado from the east (Fig. 14a, arrow). The passage of a weak surface trough across the Colorado plains between 1800 and 2100 UTC 17 February (Figs. 14a,b) prompted a shift to northerly winds east of the Rocky Mountains, bringing cooler air southward. The passage of the upper-level trough shows up very well in the profiler measurements (Figs. 3c–e). The advection of this cooler air at the surface interrupted the westward advection of the warmer, moister air into Colorado from Kansas. Additionally, a region of warm, dry air along the foothills was associated with downslope winds along the Front Range.

By 0000 UTC (Fig. 14c) a mesoscale anticyclonic circulation developed in northeast Colorado and southeast Wyoming (arrow) as strong northwesterly winds passed over the Cheyenne Ridge. This pattern changed by 0300 UTC (Fig. 14d) as the wind at Cheyenne became northerly, and dry, westerly flow dominated at Denver. By 0600 UTC, about 1 h after the mesofront arrived at the foothills, observations in eastern Colorado

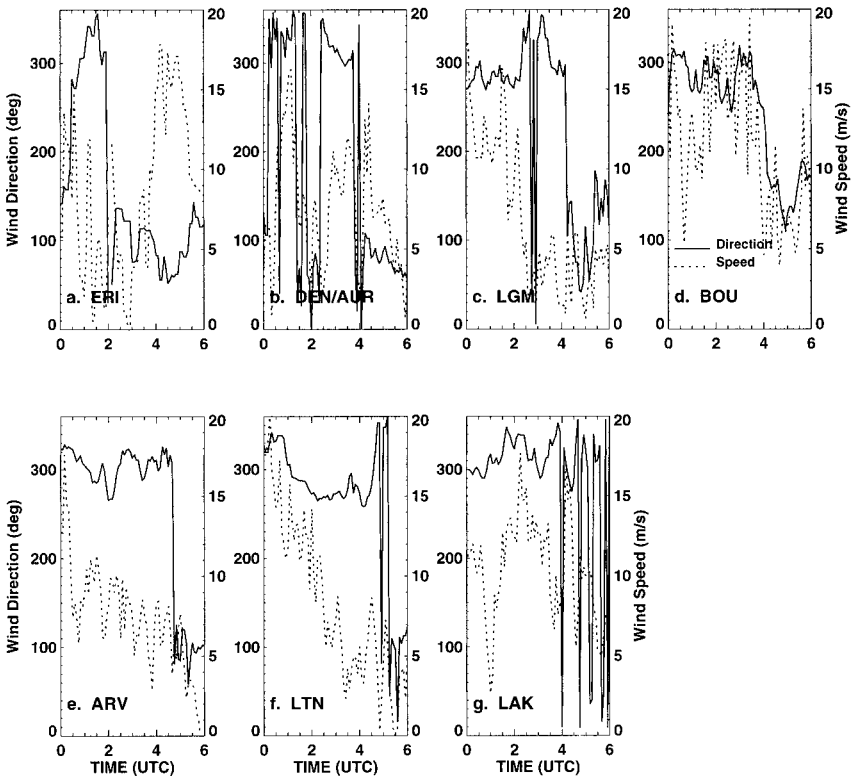

FIG. 8. Time series of wind speed (dashed) and wind direction (solid) for the same stations shown in Fig. 7.

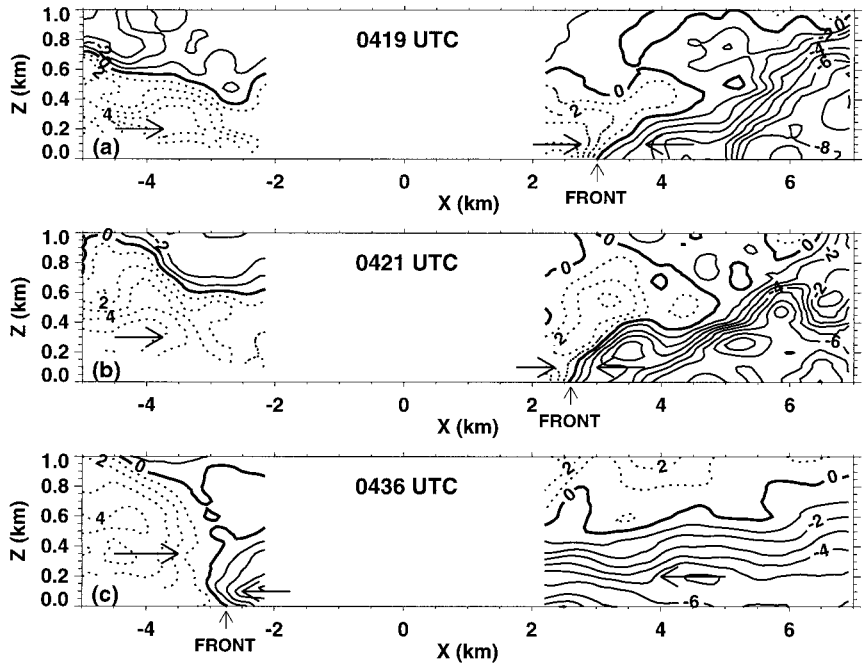

FIG. 9. Contours of the *u* component of the wind, in 1 m s^{-1} intervals. (a) and (b) Along the 70° and 250° radials. (c) Along the 60° and 240° radials. Dashed lines represent flow with a westerly component (downslope flow); solid lines represent flow with an easterly component (mesofront flow). The lidar's minimum range is 1.5 km. An additional 0.5 km on each side of the lidar was edited out because the data were noisy.

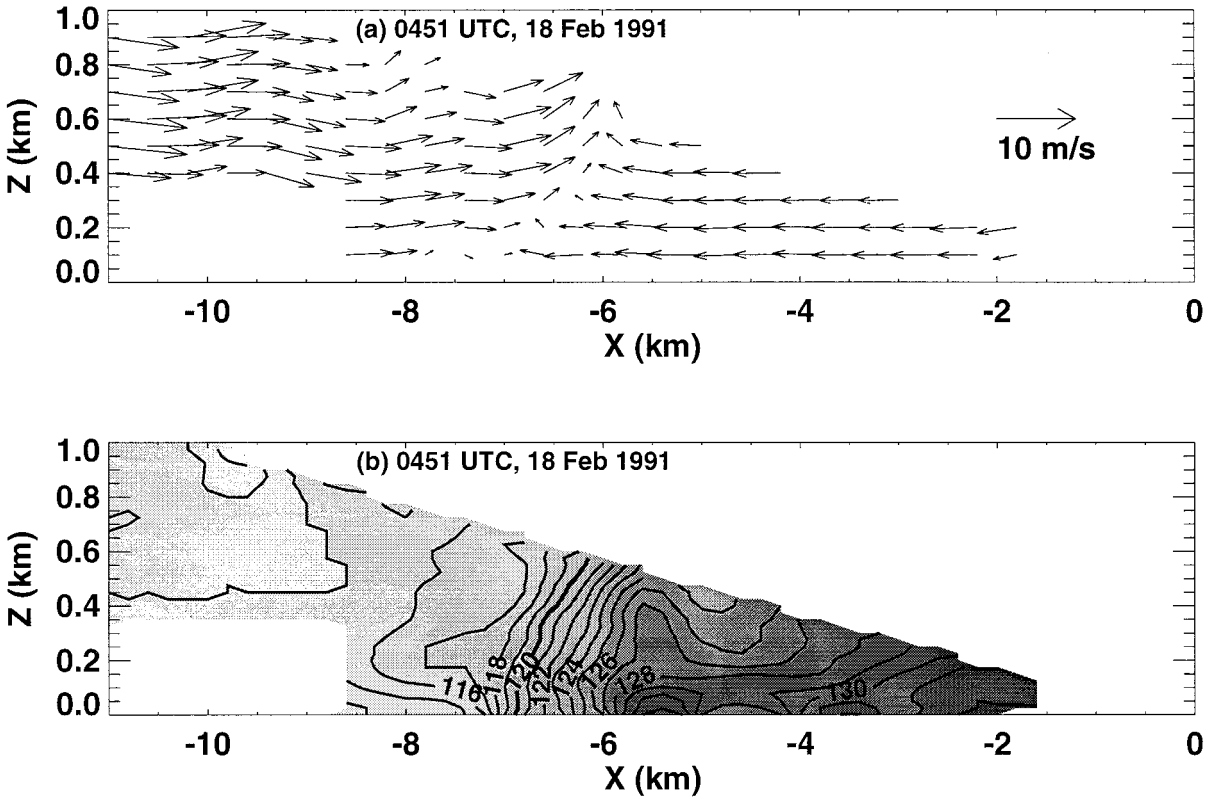

FIG. 10. Vector plot of lidar *u* and *w* components of the wind and contour plot of lidar backscattered signal intensity (dB). Higher values of signal intensity indicate a higher aerosol content in the postfrontal air mass.

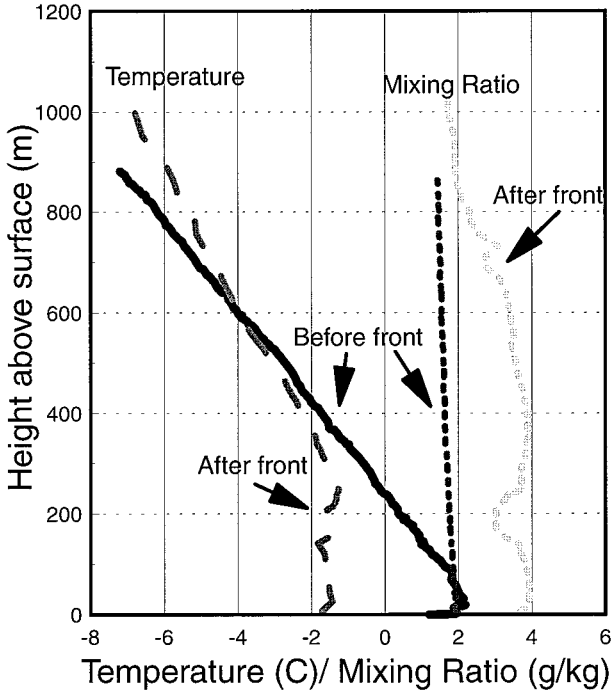

FIG. 11. Soundings launched from the lidar site.

and western Kansas showed a more uniform distribution of temperature and moisture (Fig. 14e).

6. Mesoscale analyses

Closer to the foothills, more complex flows developed as reflected in surface and boundary layer wind profiler data. For example, mesoscale surface analyses of streamlines, potential temperature, and mixing ratio, from 2200 UTC 17 February to 0600 UTC 18 February, are shown in Fig. 15. Of particular importance are the changes with time of the 3 g kg^{-1} mixing ratio contour, which is a convenient indicator of the mesofront, or boundary between the cooler, moister air on the plains, and the warmer, drier air along the foothills. For example, the east–west motion of this boundary in the ERI/BAO region coincided with wind shifts in the region. When the downslope winds increased, the boundary shifted toward the east, but when the easterly flow on the plains increased and the westerlies diminished, the boundary shifted to the west.

In late morning (1800 UTC) the winds throughout the mesonet region (not shown) had a northerly component due to surface low pressure east of Denver (Fig. 14a). With daytime solar heating, mesonet stations along the South Platte River Valley switched to northeasterly, upslope flow. Measurements from the Chatfield (CHA),

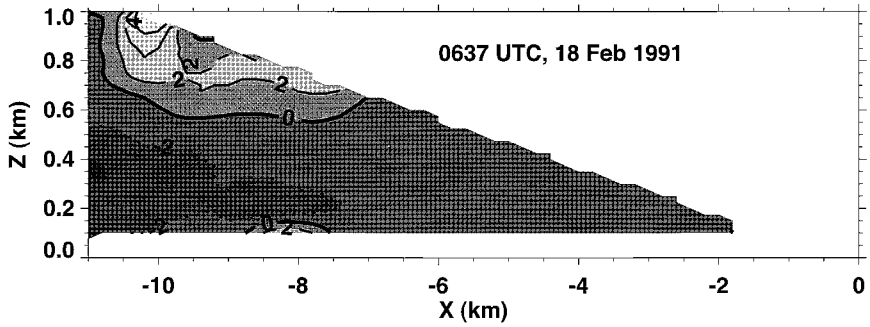

FIG. 12. Smoothed contours of the *u* component of the wind at 0637 UTC 18 Feb 1991. The lidar scanner was pointing into Eldorado Canyon.

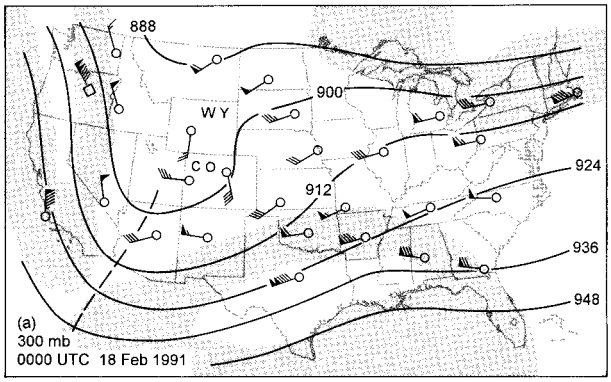

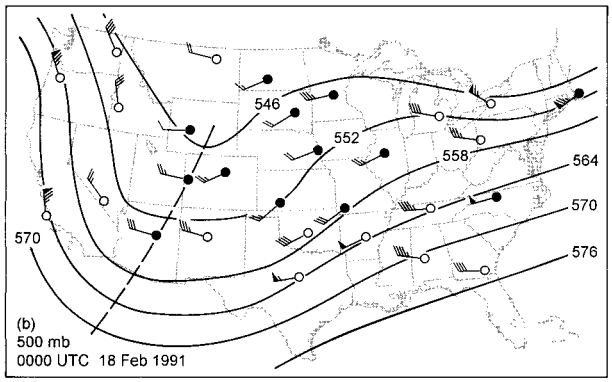

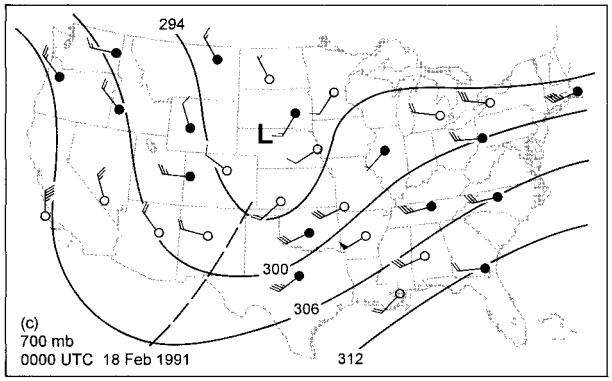

FIG. 13. Upper air synoptic maps, with standard symbols, for 0000 UTC 18 Feb 1991: (a) 300, (b) 500, and (c) 700 mb.

Adams County (ADC), and Roggin (ROG) profilers (Fig. 3) show this switch and indicate that this upslope flow was about 750 m deep. A similar pattern of upslope flow at this time of day occurred at ADC and ROG at least one-third of the time throughout the month of February 1991.

The combination of steady, strong northwesterlies on the northern plains and the upslope flow along the South Platte River Valley aided in the generation of a mesoscale anticyclonic circulation. Although the character of the circulation changed with time, in essence it existed from ~2000 UTC (17 February) throughout the evening. This circulation is locally known as the Longmont anticyclone, since the center of the circulation is typically near the Longmont (LGM) mesonet station (Wesley et al. 1995). It is often associated with the generation or intensification of precipitation, but in this case there was no precipitation. The circulation was well defined from ~2000 UTC (17 February) to 0000 UTC (18 February), with a return, or southerly flow along the foothills (Fig. 15a), similar to the event seen by Johnson et al. (1984). By 0400 UTC the circulation was much less pronounced. When the circulation became more well defined again between 0400 and 0500 UTC, the mesofront pushed westward. In addition, a decrease in the winds in the RFP region coincided with these events (Fig. 3b). These weaker downslope winds, coupled with the strengthening Longmont anticyclone, coincided with the advancement of the mesofront toward the foothills.

Profiler data showed some key features in the wind field (Fig. 3). In the evening, as westerly to northwesterly winds continued at RFP, the northeasterly upslope flow at ROG (2000–0000 UTC; Fig. 3e) was eroded away by strong northerlies on the plains by 0100 UTC, and upslope flow at CHA (2000–2100 UTC; Fig. 3c) switched to downslope flow, also by 0100 UTC. Thus, upslope flow remained all evening only at the ADC (Fig. 3d) profiler, coinciding with the easterly branch of the Longmont anticyclone.

Figure 15b, at 0100 UTC, represents the conditions that existed well before the mesofront passage at RFP. The combination of potential temperature contours, the 3 g kg^{-1} mixing ratio contour, and streamlines show

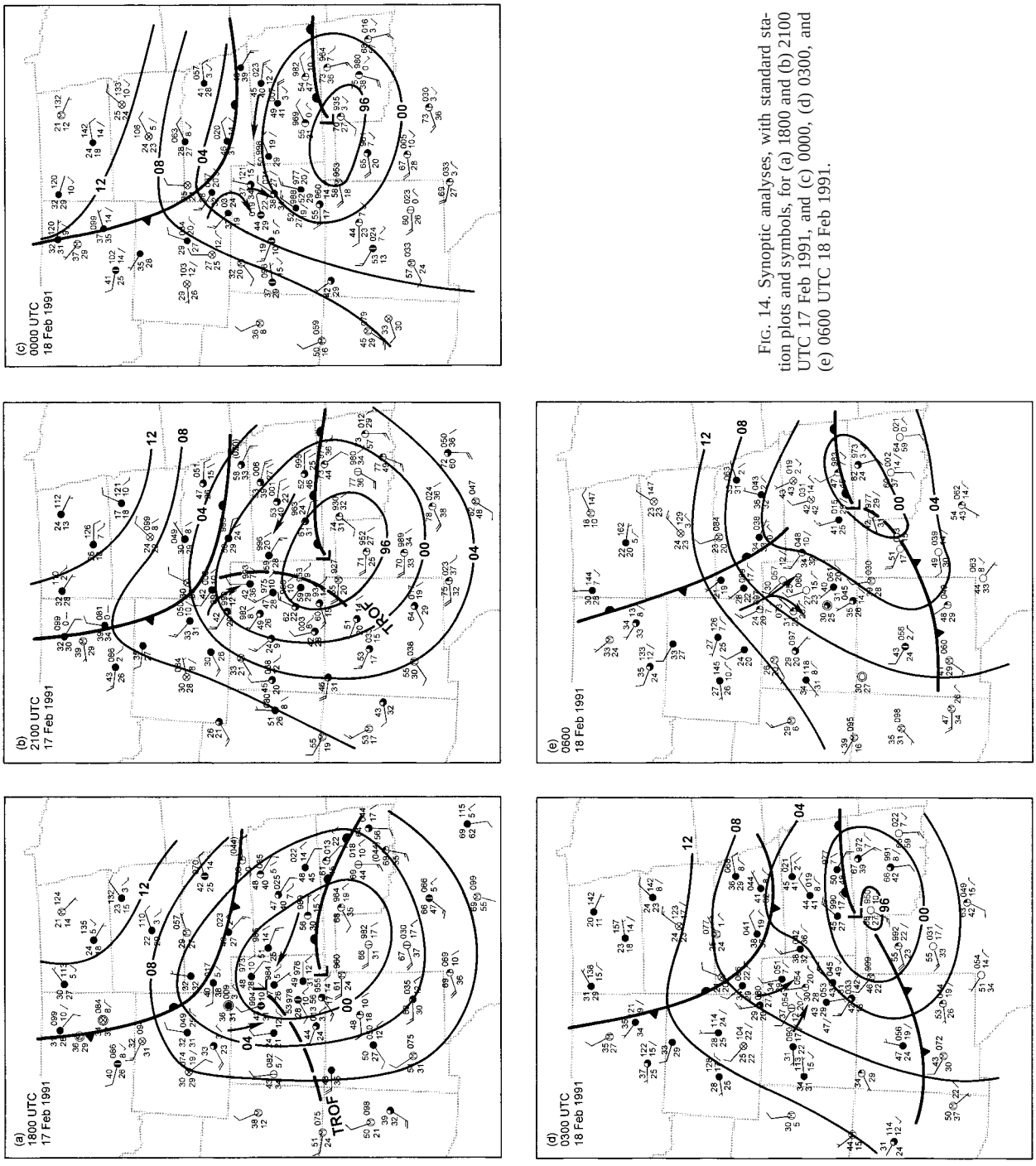

FIG. 14. Synoptic analyses, with standard station plots and symbols, for (a) 1800 and (b) 2100 UTC 17 Feb 1991, and (c) 0000, (d) 0300, and (e) 0600 UTC 18 Feb 1991.

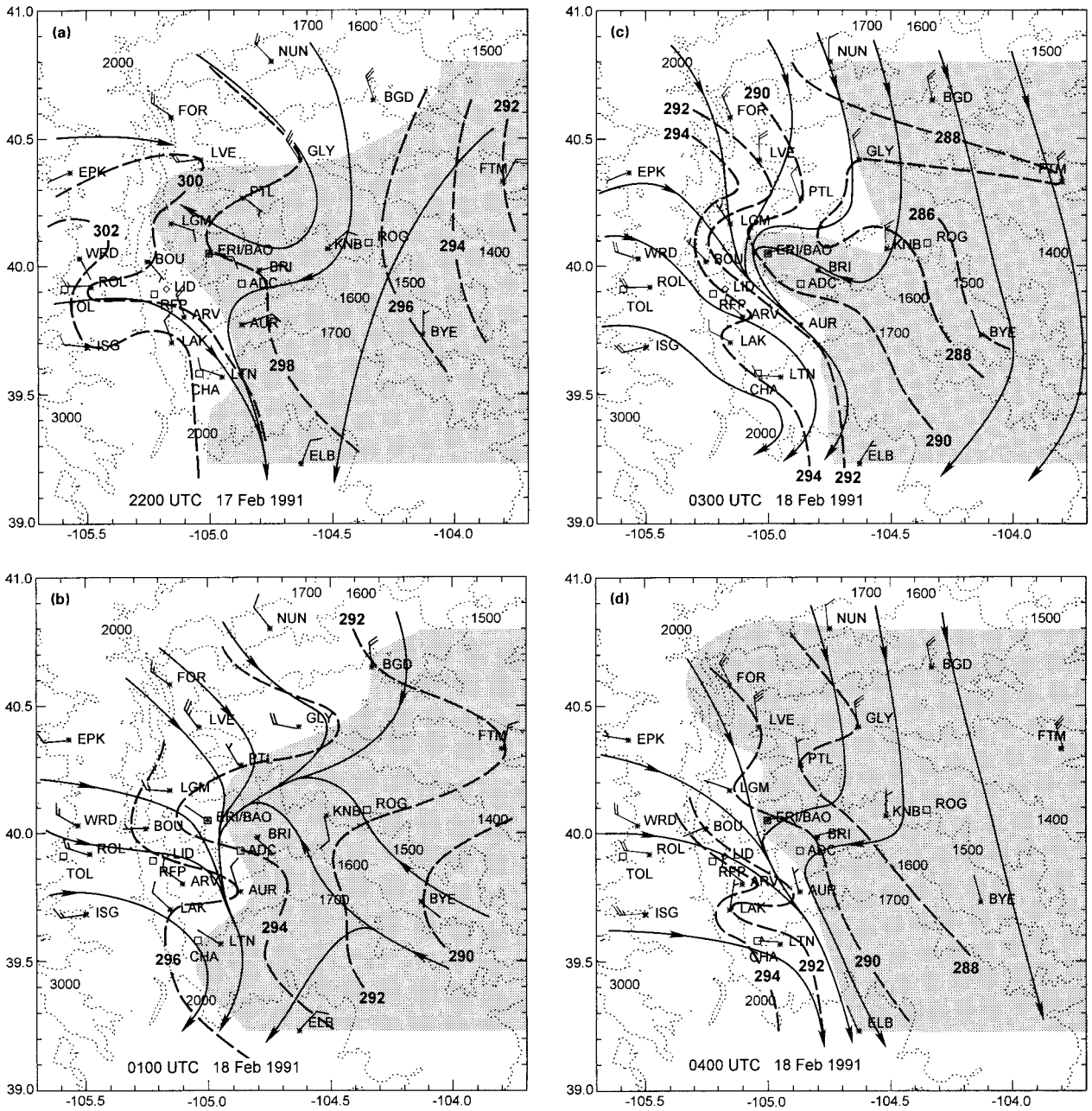

FIG. 15. Plots of 5-min averages of FSL mesonet data. Dashed lines are potential temperature, (K), solid lines are streamlines, and regions with mixing ratios ≥3 g kg^{-1} have been shaded: (a) 2200 UTC 17 Feb 1991, and (b) 0100, (c) 0300, (d) 0400, (e) 0500, and (f) 0600 UTC 18 Feb 1991.

potentially cooler, moister air being advected toward the west (center of mesonet, or near the ERI/BAO site), while the downslope winds, as seen in the Rocky Flats profiler winds, were advecting potentially warmer, dry air to the east (both north and south of the cool, moist air). This pattern remained intact throughout the evening, until the mesofront began to push toward the foothills. Upvalley flow and the convergence of winds along the South Platte River Valley were evident in the streamlines. At 0300 UTC (Fig. 15c) conditions were similar. However, as the plains stations cooled and downslope winds continued to keep stations along the foothills potentially warmer, the potential temperature gradient across the region increased slightly. The mesonet plot for 0400 UTC (Fig. 15d) showed little change in the potential temperatures, but more of the moist air mass in the northern part of the network had advected toward the foothills. The anticyclonic structure of the winds had ''relaxed.''

With the mesofront at the foothills, mesonet data for

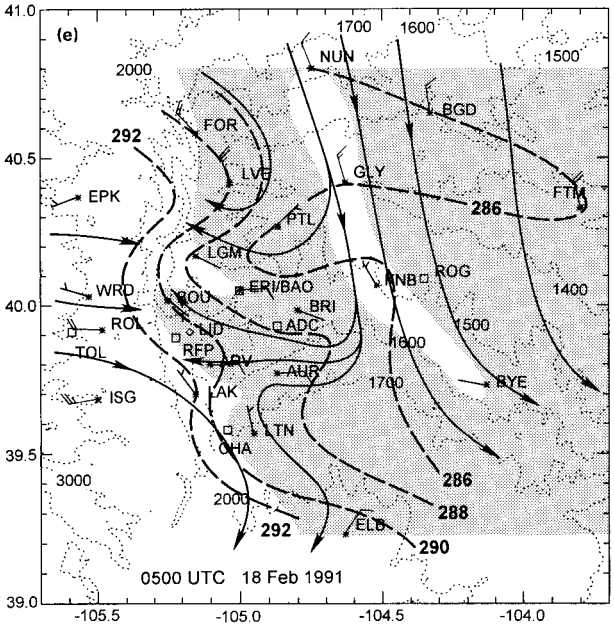

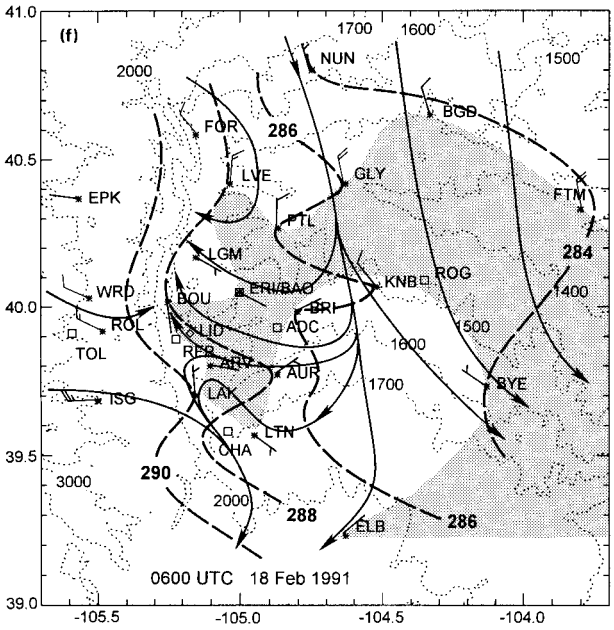

FIG. 15. (*Continued*)

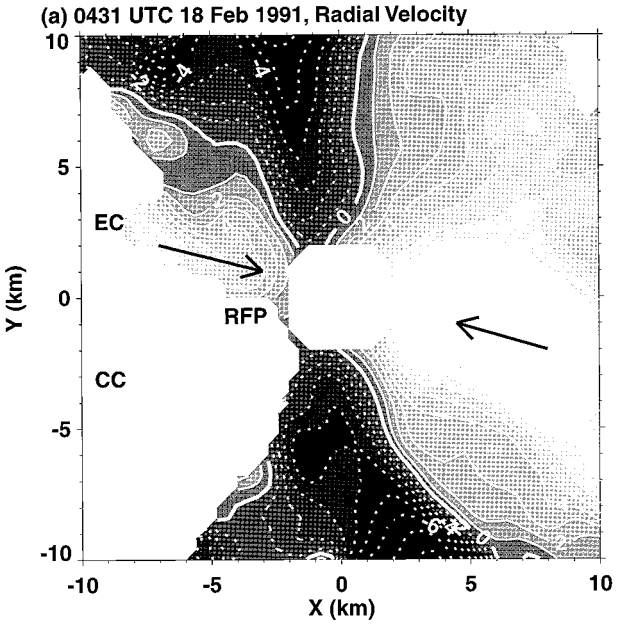

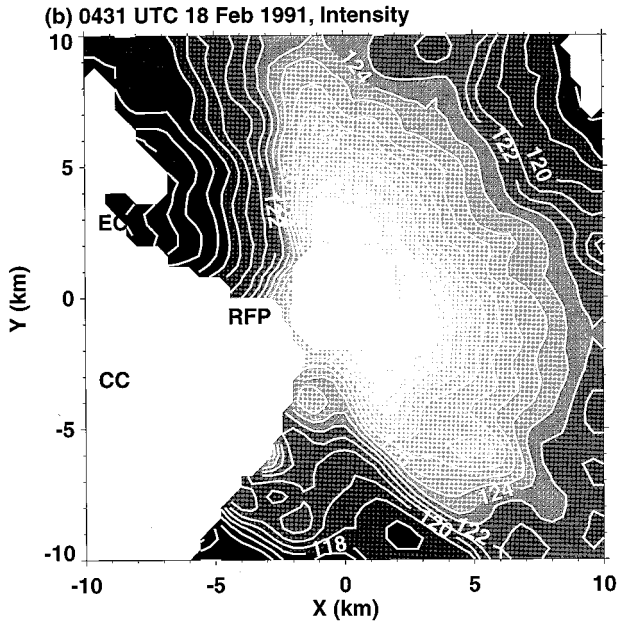

FIG. 16. Contour plots of (a) lidar radial velocity (m s^{-1}) and (b) lidar backscattered signal intensity (dB) from the 0.5° scan shown in Fig. 2c. (a) Solid lines represent flow toward the lidar (located at 0, 0) and dashed lines represent flow away from the lidar. (b) The sharp gradient in backscatter, coinciding with the zero radial velocity contour, indicates the position of the mesofront. The large data gap to the southwest is where the lidar beam intersected terrain.

0500 UTC (Fig. 15e) showed that the Longmont anticyclone had reintensified, and it stretched along the plains adjacent to the foothills, as seen in Young and Johnson (1984). Winds at Boulder (BOU) were from the south while winds in Lakewood (LAK) were from the north. More detail about this flow pattern is evident in the lidar data. In Fig. 16a, lidar radial velocity contours have been plotted for a single 0.5° PPI scan (same as scan in Fig. 2c). The accompanying backscatter plot (Fig. 16b) shows the mesofront as a strong gradient of intensity. This gradient, or delineation of the air masses, shows that the flow behind the mesofront (easterly flow) turned to the north as the westerly flow from the direction of Eldorado Canyon turned to the south.

Once the mesofront reached the foothills, the RFP profiler (Fig. 3b) showed easterly flow associated with

the mesofront below 2 km MSL. This complete change in winds at RFP due to the mesofront passage was shown in the RFP tower data (Fig. 4) to be short lived, with the easterly flow behind the mesofront lasting only ~1 h. Flow with a southerly component dominated for several hours afterward, followed by northwesterly flow.

7. Summary

Understanding the complex circulations associated with major synoptic events in complex terrain settings requires measurement of flow over a range of meteorological scales. In this study, analyses of synoptic-scale maps down to fine-resolution lidar measurements of the mesobeta front were presented, thus covering the broad range of scales tied to this event. The range of observations showed that the evolution of the mesofront proceeded as follows: Synoptic analysis showed an upper-level trough and leeside cyclogenesis at the surface. A surface low near southeast Colorado brought moist air to the plains of Colorado early in the day and downslope winds caused air near the foothills to be warm and dry. In the early evening, cooler air moved southward from Wyoming onto the Colorado plains and a boundary existed between this cooler, moister air mass and the drier, warmer air along the foothills of the Rockies. Streamline analysis of the mesonet data revealed the development and details of a well-defined Longmont anticyclone. Profilers showed the regional differences in the wind field in the lowest 1 km AGL of their measurements, including the response of leeside flows to decelerations of the large-scale winds over the Continental Divide. The maintenance of an upslope flow along the South Platte River Valley coincided with the easterly flow sector of the Longmont anticyclone. In this region, the potentially cooler and moister air was advected toward the foothills, in opposition to strong downslope flow.

High-resolution observations of this advection process, however, revealed the complex circulations that develop in complex terrain during the process of lee cyclogenesis. In particular, the boundary of moist and dry air masses moved westward and then retreated eastward a few times during the evening, resulting in an apparent ''sloshing'' of the cooler air mass over a horizontal distance of 25 km or less on the plains. Eventually the boundary between the air masses became more distinct, forming the mesofront. The sloshing pattern can be seen in the changes of mixing ratio coinciding with wind shifts at the AUR and ERI mesonet stations and the changes in position of the 3 g kg^{-1} isoline and the wind direction among the mesonet plots. It was only when the Longmont anticyclone, as shown in the mesoscale analyses, became more organized between 0400 and 0500 UTC that the mesofront was finally able to push all the way into the foothills.

Within this framework of synoptic and mesoscale measurements, NOAA/ETL Doppler lidar measurements showed in detail the vertical structure of the winds associated with the mesofront, its propagation, and the interaction between the frontal winds and the strong downslope flow along the foothills west of the RFP. Lidar measurements of the mesofront's propagation speed and the ambient flow opposing its motion, combined with RFP tower measurements, showed that the resultant Froude number was characteristic of a density current. The fact that the calculated Froude number was on the low end of the density current range is consistent with the fact that the mesofront was propagating uphill.

For emergency response applications such as those required for the RFP, the complexity of the observed winds poses a significant challenge for on-site prediction systems. In addition, the role of such mesoscale circulations is certain to be of importance in understanding the transport of polluted air along the entire Colorado Front Range in future air quality planning and assessment.

Acknowledgments. This research was sponsored by the U.S. Department of Energy as a part of the Atmospheric Studies in Complex Terrain program. We thank Richard Cupp and Ronald Willis for operating the lidar during the experiment. We appreciate Dr. Melvin Shapiro's guidance in the streamline analysis of the mesonet data and valuable discussions with Dr. F. Martin Ralph. Dr. Clark King and Dr. Shelby Frisch gave helpful reviews, and we thank the anonymous reviewers for their helpful reviews.

REFERENCES

Banta, R. M., 1995: Sea breezes shallow and deep on the California coast. *Mon. Wea. Rev.,* **123,** 3614–3622.

——, L. D. Olivier, E. T. Holloway, R. A. Kropfli, B. W. Bartram, R. E. Cupp, and M. J. Post, 1992: Smoke-column observations from two forest fires using Doppler lidar and Doppler radar. *J. Appl. Meteor.,* **31,** 1328–1349.

——, ——, and D. H. Levinson, 1993a: Evolution of the Monterey Bay sea-breeze layer as observed by pulsed Doppler lidar. *J. Atmos. Sci.,* **50,** 3959–3982.

——, ——, and P. H. Gudiksen, 1993b: Sampling requirements for drainage flows that transport atmospheric contaminants in complex terrain. *Radiat. Prot. Dosim.,* **50** (2–4), 233–248.

——, ——, W. D. Neff, D. H. Levinson, and D. Ruffieux, 1995: Influence of canyon-induced flows on flow and dispersion over adjacent plains. *Theor. Appl. Climatol.,* **52,** 27–42.

——, ——, P. Kaufmann, D. H. Levinson, and C. J. Zhu, 1999: Windflow patterns in the Grand Canyon as revealed by Doppler lidar. *J. Appl. Meteor.,* **38,** 1069–1083.

Bluestein, H. B., 1993: *Synoptic–Dynamic Meteorology in Midlatitudes.* Vol. II, *Observations and Theory of Weather Systems,* Oxford University Press, 594 pp.

Charba, J., 1974: Application of gravity current model to analysis of squall-line gust front. *Mon. Wea. Rev.,* **102,** 140–156.

Davis, C. A., 1995: Observations and modeling of a mesoscale cold surge during WISPIT. *Mon. Wea. Rev.,* **123,** 1762–1780.

——, 1997: Mesoscale anticyclonic circulations in the lee of the central Rocky Mountains. *Mon. Wea. Rev.,* **125,** 2838–2855.

Eberhard, W. L., 1992: Ice-cloud depolarization of backscatter for CO_2 and other infrared lidars. *Appl. Opt.,* **31,** 6485–6490.

Ecklund, W. Y., D. A. Carter, and B. B. Balsey, 1988: A UHF wind

profiler for the boundary layer: Brief description and initial results. *J. Atmos. Oceanic Technol.,* **5,** 432–441.

Elderkin, C. E., and P. H. Gudiksen, 1993: Transport and dispersion in complex terrain. *Radiat. Prot. Dosim.,* **50** (2–4), 265–271.

Johnson, R. H., G. S. Young, and J. J. Toth, 1984: Mesoscale weather effects of variable snow cover over northeast Colorado. *Mon. Wea. Rev.,* **112,** 1141–1152.

Koch, S. E., P. B. Dorian, R. Ferrare, S. H. Melfi, W. C. Skillman, and D. Whiteman, 1991: Structure of an internal bore and dissipating gravity current as revealed by Raman lidar. *Mon. Wea. Rev.,* **119,** 857–887.

Neff, W. D., 1990: Remote sensing of atmospheric processes over complex terrain. *Atmospheric Processes over Complex Terrain, Meteor. Monogr.,* No. 45, Amer. Meteor. Soc., 173–228.

——, 1994: Mesoscale air quality studies with meteorological remote sensing systems. *Int. J. Remote Sens.,* **15,** 393–426.

——, 1997: The Denver Brown Cloud Studies from the perspective of model assessment needs and the role of meteorology. *J. Air Waste Manage. Assoc.,* **47,** 269–285.

——, and C. W. King, 1987: Observations of complex-terrain flows using acoustic sounders: Experiments, topography, and winds. *Bound.-Layer Meteor.,* **40,** 363–392.

Post, M. J., 1986: Atmospheric purging of El Chichon debris. *J. Geophys. Res.,* **91,** 5222–5228.

——, and R. E. Cupp, 1990: Optimizing a pulsed Doppler lidar. *Appl. Opt.,* **29,** 4145–4158.

——, C. J. Grund, A. O. Langford, and M. H. Proffitt, 1992: Observations of Pinatubo ejecta over Boulder, Colorado by lidars of three different wavelengths. *Geophys. Res. Lett.,* **19,** 195–198.

Ralph, F. M., C. Mazaudier, M. Crochet, and S. V. Venkateswaran, 1993: Doppler sodar and radar wind-profiler observations of gravity-wave activity associated with a gravity current. *Mon. Wea. Rev.,* **121,** 444–463.

Shapiro, M. A., 1984: Meteorological tower measurements of a surface cold front. *Mon. Wea. Rev.,* **112,** 1634–1639.

Simpson, J. E., and R. E. Britter, 1980: A laboratory model of an atmospheric mesofront. *Quart. J. Roy. Meteor. Soc.,* **106,** 485–500.

Wesley, D. A., R. M. Rasmussen, and B. C. Bernstein, 1995: Snowfall associated with a terrain-generated convergence zone during the Winter Icing and Storms Project. *Mon. Wea. Rev.,* **123,** 2957–2977.

Young, G. S., and R. H. Johnson, 1984: Meso- and microscale features of a Colorado cold front. *J. Climate Appl. Meteor.,* **23,** 1315–1325.